

High temperature ideal Weyl semimetal phase and Chern insulator phase in ferromagnetic BaEuNiOsO₆ and its (111) (BaEuNiOsO₆)/(BaTiO₃)₁₀ superlattice

Hai-Shuang Lu¹ and Guang-Yu Guo^{2,3,*}

¹*School of Electronic and Information Engineering,*

Changshu Institute of Technology, Changshu 215500, People's Republic of China

²*Department of Physics, National Taiwan University, Taipei 10617, Taiwan*

³*Physics Division, National Center for Theoretical Sciences, Taipei 10617, Taiwan*

Weyl semimetals (WSMs) have recently stimulated intensive interest because they exhibit fascinating physical properties and also promise exciting technological applications. So far, however, the few confirmed magnetic WSMs generally have a large number of Weyl points either located away from the Fermi level (E_F) or shrouded by nontopological Fermi surface pockets. Based on first-principles density functional theory calculations, we establish cubic double perovskite BaEuNiOsO₆ to be a high Curie temperature (T_c) ferromagnetic WSM with magnetization along the [111] direction, just two pairs of Weyl points at the E_F and $T_c = 325$ K. The strong ferromagnetism is attributed to the strong ferromagnetic Ni 3d-Eu 4f-Os 5d coupling induced by the substitution of half of Ba atoms with Eu atoms in double perovskite Ba₂NiOsO₆. Moreover, the momentum separation of one Weyl point pair is large, thus giving rise to not only a long (001) surface Fermi arc but also large anomalous Hall conductivity. Intriguingly, as a unique physical result of a ferromagnetic WSM, the (111) BaEuNiOsO₆ monolayer superlattice (BaEuNiOsO₆)/(BaTiO₃)₁₀, being its (111) quantum-well structure, is found to be a high temperature ($T_c = 210$ K) Chern insulator with a large band gap of ~ 90 meV. Therefore, cubic double perovskite BaEuNiOsO₆ will provide a superior high temperature material platform for exploring fundamental physics of Weyl fermions and its (111) monolayer superlattices will offer a high temperature magnetic topological insulator for studying exotic quantum phenomena such as quantum anomalous Hall effect.

I. INTRODUCTION

Weyl semimetals (WSMs), hosting Weyl fermions described by the Weyl Hamiltonian [1], have attracted extensive interest due to their unusual physical properties and potential technological applications [2–7]. In a WSM, the conduction and valence bands disperse linearly through the Weyl points in the Brillouin zone (BZ). The Weyl points behave as the monopoles of Berry curvature with opposite chiralities and connect the two ends of the nonclosed surface Fermi arcs [8–13]. Magnetic WSMs with broken time-reversal symmetry are especially interesting. They provide a playground for the interplay among magnetism, symmetry and topology, which can give rise to exotic quantum phenomena such as chiral magnetic effect [14, 15], large universal anomalous Hall effect (AHE) [16], low-frequency divergent bulk photovoltaic effect [17] and also quantum anomalous Hall effect (QAHE) [18]. Although a number of magnetic WSMs candidates have been proposed, e.g. pyrochlore iridate Y₂Ir₂O₇ [2], spinel compounds HgCr₂Se₄ [18] and VMg₂O₄ [19], half-Heusler RPtBi ($R = \text{Gd}$ and Nd) [20, 21], certain Co₂-based Heusler compounds [22–25], ferromagnetic (FM) kagome-lattice Co₃Sn₂S₂ [16, 26, 27], and noncentrosymmetric RAlGe family of compounds ($R = \text{rare earth elements}$) [28, 29], few have been confirmed by experiments [25–27, 29]. Furthermore, in the few confirmed WSMs, there are usually

a large number of Weyl points located either far above or below the Fermi level and also shrouded by nontopological Fermi surface pockets [16, 25, 28]. This certainly hinders the studies of the exotic properties especially novel transport phenomena in WSMs. Therefore, it is highly desirable to find high Curie temperature (T_c) magnetic WSMs with only a couple of pairs of Weyl points located at or close to the Fermi level (so-called ideal WSMs) [30].

Transition metal oxide perovskites (ABO₃) and also double perovskites A₂BB'O₆ possess high cubic symmetries and exhibit a rich variety of fascinating properties such as colossal magnetoresistance and half-metallic behavior [31]. Their atomic scale heterostructures offer the prospect of further enhancing these fascinating properties or of combining them to realize exotic properties and functionalities [32, 33]. Recently, based on their tight-binding (TB) modelling and density functional theory (DFT) calculations, Xiao *et al.* showed in their seminal paper [34] that various quantum topological phases could appear in a class of (111) perovskite bilayers (BLs) sandwiched by insulating perovskites where transition metal atoms in the BLs form a buckled honeycomb lattice. Subsequently, the electronic structures of a large number of (111) perovskite BLs and also double-perovskite monolayers (MLs) in the (111) oxide superlattices were investigated and some of them were predicted to host quantum spin Hall, quantum anomalous Hall (QAH) and other topological phases (see, e.g., Ref. [35] and references therein). In particular, (111) perovskite BLs [36–41] and also (111) double perovskite MLs [42, 43] have been predicted to be QAH insulators.

However, very few magnetic WSMs based on oxide

*Electronic address: gyguo@phys.ntu.edu.tw

perovskite or double perovskite structures have been reported [44], despite a lot of magnetic WSMs based other materials have been predicted, as mentioned above. We notice that a magnetic WSM can be viewed as a stack of two-dimensional QAH insulators with strong coupling in the stacking direction [2, 18, 35, 45]. This naturally leads to a "inverse engineering" strategy for finding magnetic WSM phases in bulk perovskites and double perovskites. One first looks for high T_c QAH phases in perovskite BLs or double perovskite MLs. One then examines possible magnetic WSM phases in the corresponding bulk perovskites and double perovskites.

In this work, as a continuation of our endeavor in searching for high T_c QAH phases in perovskite BLs [40] and also in double perovskite MLs [46], we study the electronic structure of the (111) ML of Eu-doped double perovskite $\text{Ba}_2\text{NiOsO}_6$. Double perovskite $\text{Ba}_2\text{NiOsO}_6$ is a rare FM semiconductor with T_c of 100 K [47]. Our previous DFT calculation revealed that the ferromagnetism is driven by the FM coupling between Ni and Os atoms [46], which is very rare between the B and B' in double perovskites [48]. Furthermore, our previous calculation showed that its energy bands near the Fermi level are dominated by Os $5d$ t_{2g} orbitals with t_{2g}^2 electron configuration [46]. Consequently, the strong spin-orbit coupling (SOC) on the heavy Os atom opens the semiconducting gap, thus making $\text{Ba}_2\text{NiOsO}_6$ a so-called Dirac semiconductor [46, 47]. According to Ref. [34], the (111) double perovskite MLs with t_{2g}^1 , t_{2g}^2 , t_{2g}^3 and t_{2g}^4 electronic configurations are all possible topological materials. Previously, we found that the first band gap below the valence band maximum in the (111) $\text{Ba}_2\text{NiOsO}_6$ ML is topologically nontrivial, although it is an ordinary FM semiconductor with a predicted T_c of 70 K [46]. Now, if one A-site atom in $\text{Ba}_2\text{NiOsO}_6$ is replaced by a magnetic $4f$ atom, forming additional FM coupling channels, its ferromagnetism could be further strengthened, resulting in a higher T_c . Moreover, such A-site substitution would break the spatial inversion symmetry of both bulk $\text{Ba}_2\text{NiOsO}_6$ and its (111) ML, thus leading to the possible emergence of topological phases.

Indeed, as will be presented in Sec. III, our DFT calculations indicate that the (111) $(\text{BaEuNiOsO}_6)/(\text{BaTiO}_3)_{10}$ ML superlattice is a Chern insulator with high T_C of 210 K. Furthermore, our calculations also reveal that bulk BaEuNiOsO_6 is a FM WSM with high T_C of 325 K and two pairs of Weyl points at the Fermi level only. In other words, guided by the inverse engineering strategy, we discover that bulk BaEuNiOsO_6 is a rare ideal ferromagnetic WSM. Therefore, double-perovskite BaEuNiOsO_6 will provide a superior platform for exploring fascinating Weyl fermion physics and its (111) ML superlattice and its (111) ML superlattice will be a high temperature Chern insulator for studying exotic quantum phenomena such as QAH effect. The rest of this paper is organized as follows. In the next section, a brief description of the crystalline structures of bulk BaEuNiOsO_6 and its

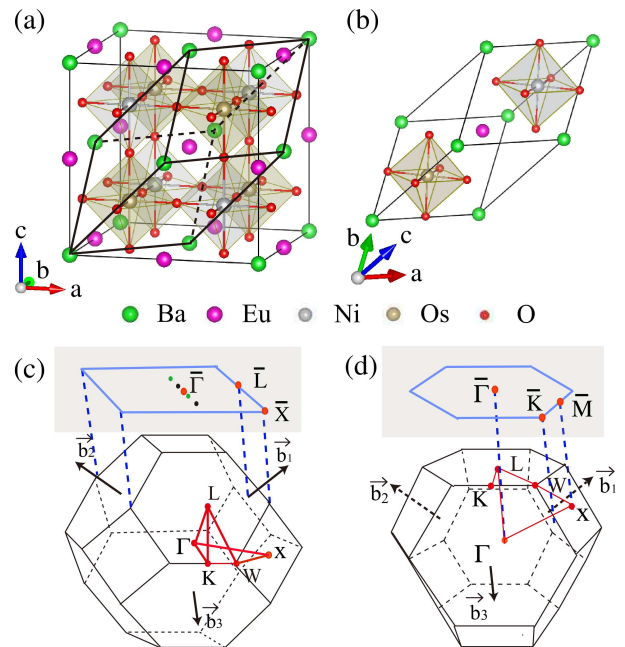


FIG. 1: Cubic crystal structure of bulk BaEuNiOsO_6 . (a) Conventional cubic cell and (b) fcc primitive cell as well as the associated fcc Brillouin zone (BZ) with (c) the corresponding (001) surface BZ and (d) the corresponding (111) surface BZ. In (a), the black lines indicate the fcc primitive cell (b). In (c) and (d), \vec{b}_1 , \vec{b}_2 and \vec{b}_3 are the reciprocal lattice vectors.

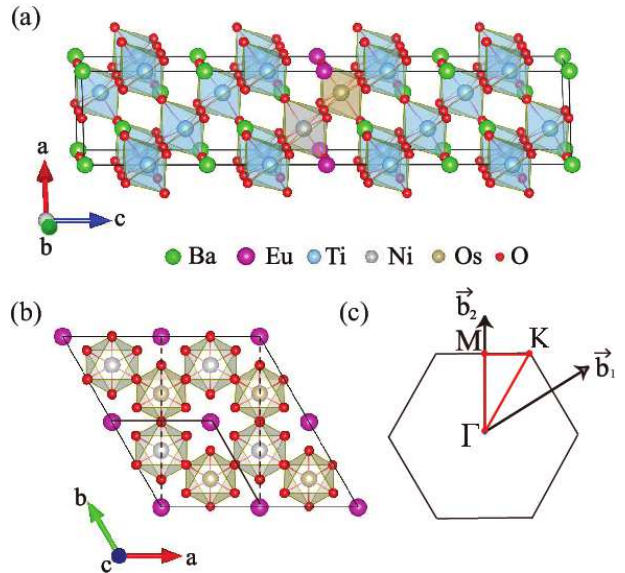


FIG. 2: Crystal structure of the (111) $(\text{BaEuNiOsO}_6)/(\text{BaTiO}_3)_{10}$ superlattice. (a) Side view along the b -axis, (b) top view along the c -axis and (c) the corresponding two-dimensional (2D) BZ. In (b), the black lines denote the 2D primitive cell. In (c), \vec{b}_1 and \vec{b}_2 represent the 2D reciprocal lattice vectors.

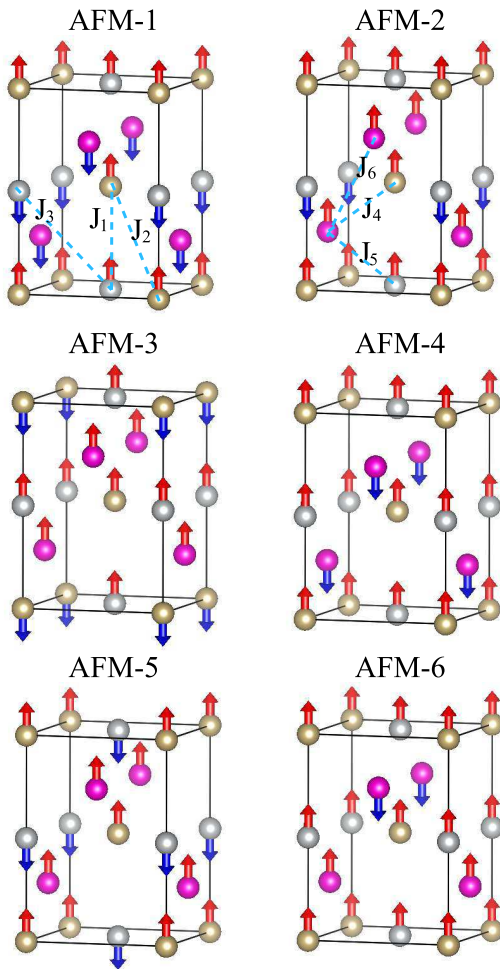


FIG. 3: Six considered antiferromagnetic configurations (AFM- i) in bulk BaEuNiOsO₆.

(111) ML superlattice as well as the used theoretical methods and computational details is given. In Sec. III, the calculated magnetic properties and electronic band structures as well as the uncovered quantum topological phases are presented. Finally, the conclusions drawn from this work are summarized in section IV.

II. THEORY AND COMPUTATIONAL DETAILS

We consider face-centered-cubic double perovskite BaEuNiOsO₆ with noncentrosymmetric space group $F\bar{4}3m$ (No. 216) (see Fig. 1), and also its (111) ML sandwiched by an insulating perovskite BaTiO₃ slab as in the (BaEuNiOsO₆)/(BaTiO₃)₁₀ superlattice grown along the [111] direction (see Fig. 2). The resultant ML superlattice is a trigonal structure [space group $P\bar{3}m1$ (C_{3v}^1), no. 156] without spatial inversion symmetry. In each (111) BaEuNiOsO₆ ML, Ni and Os atoms form a buckled honeycomb lattice separated by an EuO₃ layer. The Brillouin zones of bulk BaEuNiOsO₆ and the (111) ML are shown in Figs. 1(c) and 1(d) and Fig. 2(c), respec-

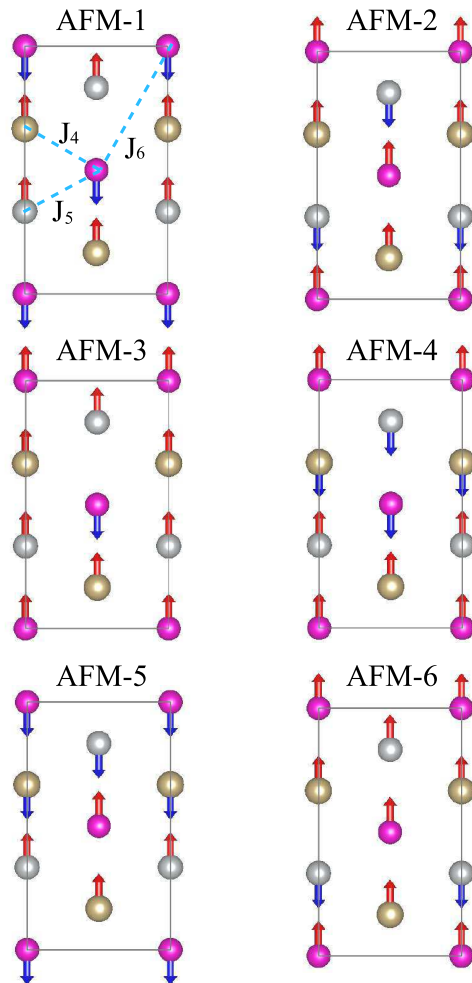


FIG. 4: Six considered antiferromagnetic configurations (AFM- i) in the (111) BaEuNiOsO₆ monolayer in the (111) (BaEuNiOsO₆)/(BaTiO₃)₁₀ superlattice. The cell here is indicated by the dashed lines in Fig. 2(b).

tively. Clearly, the latter is the folded BZ of the former along the Γ -L direction. Since the BaTiO₃ slab in the (BaEuNiOsO₆)/(BaTiO₃)₁₀ superlattice is much thicker than the BaEuNiOsO₆ ML, the BaTiO₃ slab could be regarded as the substrate. Therefore, in the present structural optimization calculation, the in-plane lattice constant is fixed at $\sqrt{2}a_0 = 5.6962$ Å, where $a_0 = 4.0278$ Å is the theoretically determined lattice constant of cubic BaTiO₃, while the lattice constant c and the internal coordinates of all the atoms in the superlattice are then optimized theoretically. Also, the theoretically determined lattice parameters and atom positions for both cases are shown, respectively, in Tables S1 and S2 for bulk BaEuNiOsO₆ and also in Table S3 for the (BaEuNiOsO₆)/(BaTiO₃)₁₀ superlattice in the Supplementary Materials (SM) [49]. It is worth noting that the primitive unit cell [see Fig. 1(b)] is used in all the present calculations for bulk cubic BaEuNiOsO₆.

The present electronic and magnetic structure as well

as structural optimization calculations are based on the DFT with the generalized gradient approximation (GGA) [50]. The accurate projector-augmented wave (PAW) method [51], as implemented in the Vienna *ab initio* simulation package (VASP) [52], is used. The relativistic PAW potentials are adopted in order to include the SOC. The valence configurations of Ba, Eu, Ni, Os, Ti and O atoms adopted in the present calculations are $5s^25p^66s^2$, $5s^25p^64f^76s^2$, $3p^63d^84s^2$, $5p^65d^66s^2$, $3s^23p^63d^24s^2$ and $2s^22p^4$, respectively. To better account for the on-site electron correlation on the Os $5d$, Ni $3d$ and Eu $4f$ shells, the GGA+U method [53] is adopted with the effective Coulomb repulsion energies $U_{Os} = 2.0$ eV, $U_{Ni} = 5.0$ eV, and $U_{Eu} = 4.0$ eV. These U values were found appropriate for perovskite oxide EuTiO_3 [54] and double-perovskite oxide $\text{Ba}_2\text{NiOsO}_6$ [46] in our earlier works [46, 54]. In particular, the GGA+U calculation with $U_{Eu} = 4.0$ eV correctly predicted bulk EuTiO_3 to be a G-type antiferromagnetic insulator with the Neel temperature $T_N = 6.0$ K. [54] A large plane-wave cutoff of 400 eV and the small total energy convergence criterion of 10^{-5} eV are used throughout. Fine Monkhorst-Pack k -meshes of $50 \times 50 \times 50$ and $10 \times 10 \times 2$ are used for the BZ integrations for bulk BaEuNiOsO_6 and the ML superlattice, respectively. In the structural optimizations, ferromagnetic GGA+U scalar-relativistic calculations are performed.

To find the ground state magnetic configuration and to understand the magnetic interactions in bulk $\text{Ba}_2\text{NiOsO}_6$ and its (111) ML, we consider seven possible magnetic structures for each system including the ferromagnetic structure and six antiferromagnetic (AFM) structures as shown in Figs. 3 and 4, respectively. One can then evaluate the nearest-neighbor Ni-Os (J_1), Os-Os (J_2), Ni-Ni (J_3), Eu-Os (J_4), Eu-Ni (J_5) and Eu-Eu (J_6) magnetic coupling parameters by mapping the calculated total energies of the seven magnetic configurations to the classical Heisenberg model $H = E_0 - \sum_{i>j} J_{ij}(\hat{e}_i \cdot \hat{e}_j)$, where J_{ij} is the exchange coupling parameter between sites i and j , and \hat{e}_i is the unit vector indicating the direction of spin on site i (see supplementary note 1 in the SM [49]). Based on the calculated J values, we could estimate magnetic ordering temperature (T_c) within a mean-field approximation given by $k_B T_c = \frac{1}{3} \sum_i z_i J_i$ where z_i are the numbers of Ni-Os, Os-Os, Ni-Ni, Eu-Os, Eu-Ni and Eu-Eu pairs (bonds) in the considered system (see supplementary note 1 in the SM).

The anomalous Hall conductivity (AHC) is calculated based on the Berry-phase formalism [55]. Within this Berry-phase formalism, the AHC ($\sigma_{ij}^A = J_i^c/E_j$) is given as a BZ integration of the Berry curvature for all the occupied (valence) bands,

$$\sigma_{xy}^A = -\frac{e^2}{\hbar} \sum_{n \in VB} \int_{BZ} \frac{d\mathbf{k}}{(2\pi)^3} \Omega_{xy}^n(\mathbf{k}),$$

$$\Omega_{xy}^n(\mathbf{k}) = \nabla_{\mathbf{k}} \times \langle u_{n\mathbf{k}} | i \nabla_{\mathbf{k}} | u_{n\mathbf{k}} \rangle, \quad (1)$$

where $\Omega_{ij}^n(\mathbf{k})$ and $u_{n\mathbf{k}}$ are, respectively, the Berry cur-

TABLE I: Calculated total energies (E_{FM} , E_{AFM-i}) of the FM and six considered AFM states (see Figs. 3 and 4) with the GGA+U method, exchange coupling parameters (J_i) and also the estimated magnetic ordering temperature (T_c) of bulk BaEuNiOsO_6 and its (111) monolayer in the (111) $(\text{BaEuNiOsO}_6)/(\text{BaTiO}_3)_{10}$ superlattice. Here J_1 (d_{Ni-Os}), J_2 (d_{Os-Os}), J_3 (d_{Ni-Ni}), J_4 (d_{Eu-Os}), J_5 (d_{Eu-Ni}), and J_6 (d_{Eu-Eu}) represent the nearest Ni-Os, Os-Os, Ni-Ni, Eu-Os, Eu-Ni and Eu-Eu exchange coupling parameter (interatomic distance), respectively.

	Bulk	(111) monolayer
E_{FM} (meV/f.u.)	0	0
E_{AFM-1} (meV/f.u.)	133.325	28.39
E_{AFM-2} (meV/f.u.)	51.55	31.99
E_{AFM-3} (meV/f.u.)	106.075	4.575
E_{AFM-4} (meV/f.u.)	105.26	38.84
E_{AFM-5} (meV/f.u.)	105.695	42.90
E_{AFM-6} (meV/f.u.)	26.085	18.455
d_{Ni-Os} (Å)	3.965	4.016
d_{Os-Os} (Å)	5.607	5.696
d_{Ni-Ni} (Å)	5.607	5.696
d_{Eu-Os} (Å)	3.434	3.495
d_{Eu-Ni} (Å)	3.434	3.475
d_{Eu-Eu} (Å)	5.607	5.696
J_1 (meV)	8.186	3.981
J_2 (meV)	1.492	6.468
J_3 (meV)	-0.162	0.615
J_4 (meV)	10.222	3.381
J_5 (meV)	-0.102	1.351
J_6 (meV)	-3.121	-2.405
T_c (K)	~ 325 ($\sim 100^a$)	~ 210 ($\sim 69^b$)

^aExperimental value of bulk $\text{Ba}_2\text{NiOsO}_6$ from Ref. [47].

^bCalculated value for (111) $\text{Ba}_2\text{NiOsO}_6$ monolayer from Ref. [46].

vature and cell periodic wave function for the n th band at \mathbf{k} . J_i^c is the i -component of the charge current density \mathbf{J}^c and E_j is the j -component of the electric field \mathbf{E} . Since a large number of k points are needed to get accurate AHCs, we use the efficient Wannier interpolation method [56, 57] based on maximally localized Wannier functions (MLWFs) [58]. Since the energy bands around the Fermi level are dominated by Os $5d$ t_{2g} and Eu $4f$ orbitals, 24 MLWFs are constructed by fitting to the GGA+U+SOC band structures. The band structures obtained by the Wannier interpolation agree well with that from the GGA+U+SOC calculations (see Fig. S1 in the SM). The AHC (σ_{xy}^A) is then evaluated by taking very dense k -point meshes of $250 \times 250 \times 250$ and $200 \times 200 \times 2$ for bulk BaEuNiOsO_6 and its (111) ML, respectively. The surface states of bulk $\text{Ba}_2\text{NiOsO}_6$ and the edge states of the (111) $\text{Ba}_2\text{NiOsO}_6$ ML are calculated by the Green function technique [59, 60], as implemented in the WannierTools code [61].

TABLE II: Calculated spin (m_s) and orbital (m_o) magnetic moments as well as band gap (E_g) and anomalous Hall conductivity (σ_{xy}^A) of FM bulk BaEuNiOsO₆ with magnetization along the (111) direction and its (111) monolayer in the (111) (BaEuNiOsO₆)/(BaTiO₃)₁₀ superlattice with the perpendicular magnetization using the GGA+U+SOC method. Also listed are the Eu f - as well as Os and Ni d -shell configurations. For bulk BaEuNiOsO₆, σ_{xy}^A is calculated at the energy level of the Weyl points.

	Bulk	(111) monolayer
Eu _{vc}	4 f^7	4 f^7
Os _{vc}	5 d^2 (t_{2g}^2)	5 d^2 (t_{2g}^2)
Ni _{vc}	3 d^8 ($t_{2g}^6 e_g^2$)	3 d^8 ($t_{2g}^6 e_g^2$)
m_s^{Os} (μ_B /atom)	1.499	1.463
m_o^{Os} (μ_B /atom)	-0.367	-0.345
m_s^{Ni} (μ_B /atom)	1.768	1.747
m_o^{Ni} (μ_B /atom)	0.213	0.209
m_s^{Ti} (μ_B /atom)	-	0.012
m_o^{Ti} (μ_B /atom)	-	-0.003
m_s^O (μ_B /atom)	0.095	0.100
m_o^O (μ_B /atom)	-0.061	-0.014
m_s^{Eu} (μ_B /atom)	6.717	6.670
m_o^{Eu} (μ_B /atom)	-0.473	-0.566
m_t^{Eu} (μ_B /atom)	6.244	6.104
m_t^{Os} (μ_B /atom)	1.132	1.118
m_t^{Ni} (μ_B /atom)	1.981	1.956
E_g (eV)	0	0.093
σ_{xy}^A (e^2/hc)	-1.122	-1.000

III. RESULTS AND DISCUSSION

A. Magnetic properties

The calculated total energies of the seven considered magnetic configurations for both systems are listed in Table I. These energies are calculated by the GGA + U method with $U_{Os} = 2.0$ eV, $U_{Ni} = 5.0$ eV, and $U_{Eu} = 4.0$ eV. For both structures, the FM configuration is the ground state. As mentioned before, using these total energies, we evaluate the exchange coupling parameters J_1 , J_2 , J_3 , J_4 , J_5 and J_6 (see supplementary note 1 in the SM [49]), as listed in Table I together with the corresponding atom-atom distances. For bulk BaEuNiOsO₆, the obtained J_1 , J_2 and J_4 are positive (ferromagnetic), while J_3 , J_5 and J_6 are negative (antiferromagnetic). Furthermore, the magnitudes of J_1 and J_4 are much larger than that of all other parameters including J_3 , J_5 and J_6 . This means that ferromagnetism in bulk BaEuNiOsO₆ is caused by the strong FM couplings between neighboring Os and Ni atoms (J_1) as well as between neighboring Os and Eu atoms (J_4). Compared with J_1 and J_4 , the sizes of J_3 and J_5 are negligibly small. The smallness of J_3 could be attributed to the much localized Ni $3d$ orbitals and also the much larger separation of the neighboring Ni atoms (see Table I). The smallness of J_5 could result from the much weaker Ni $3d$ -Eu $4f$ hybridization due to the much localized Ni $3d$ as well as Eu $4f$ orbitals. Inter-

estingly, Table I indicates that J_3 and J_5 become positive in the (111) BaEuNiOsO₆ monolayer. Table I also shows that in the monolayer, J_2 is enhanced by a factor of 4 and thus becomes dominant while J_1 and J_4 get reduced by a factor of 2 and 3, respectively. All these suggest that ferromagnetism in the monolayer is caused by strong FM couplings between neighboring Os atoms (J_2) as well as between neighboring Os and Ni atoms (J_1) and between neighboring Os and Eu atoms (J_4).

In both BaEuNiOsO₆ structures, due to the presence of magnetic Eu atoms which are staggered between the Ni and Os atoms, the number of magnetic coupling channels increases. Compared with Ba₂NiOsO₆, the additional coupling channels from Eu $4f$ to Os $5d$ in the BaEuNiOsO₆ structures not only are of FM type (see Table I), thus enhancing the overall FM exchange coupling strength, but also are the principal magnetic couplings. This results in a substantial increase of T_c and thus the estimated T_c value is as high as 325 K for bulk BaEuNiOsO₆ and 210 K for its monolayer, being much larger than that of 150 K and 69 K in bulk Ba₂NiOsO₆ and its (111) monolayer [46, 47], respectively. Nonetheless, it should be noted that the mean-field estimation of the magnetic transition temperature works rather well only for the systems where the magnetic atoms are coupled to a large number of neighboring magnetic atoms. This is often not the case for real magnetic materials, and thus the transition temperature is generally overestimated by the mean-field approach (MFA), especially for low-dimensional materials. We do notice that in an earlier study on bulk EuTiO₃ [54], the GGA+U calculation plus the MFA correctly predicted bulk EuTiO₃ to be a G-type antiferromagnetic insulator with $T_N = 6$ K [54]. Therefore, we believe that the estimated T_C value for bulk BaEuNiOsO₆ may be slightly too high, while that of its (111) ML superlattice would be significantly too high.

We notice that although magnetic topological insulating phases have been proposed in many materials, so far there have been few experimental reports on the observation of such topological phases [35, 62]. Weak magnetic coupling and hence low T_c values have been considered as a key factor that hinders the experimental observation of these topological phases. [40, 41] Therefore, some schemes have been proposed to increase T_c . One proposed route is to exploit the proximity effect coupling the surface states of a nonmagnetic topological insulator (TI) directly with a high T_c magnetic insulator [63, 64]. An alternative route is to optimize the transition metals in the considered systems. For example, it was proposed in Refs. [40, 41] to replace some B-site $3d$ transition metal atoms in the (111) ABO₃ perovskite bilayers with $4d$ and $5d$ atoms which simultaneously have more extended d orbitals and stronger SOC. Here we offer another way to enhance the T_c by substitution of A-site atoms with $4f$ magnetic atoms in transition metal perovskite oxides.

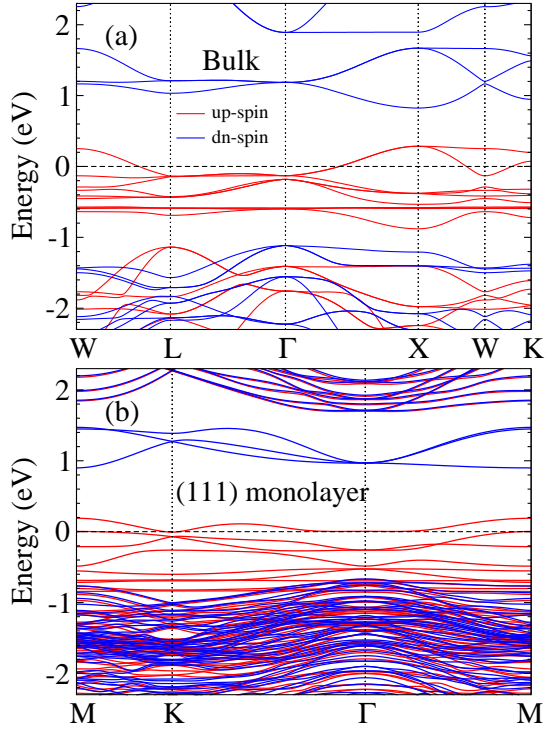


FIG. 5: Scalar-relativistic band structures of (a) bulk BaEuNiOsO₆ and (b) the (111) (BaEuNiOsO₆)/(BaTiO₃)₁₀ superlattice obtained with the GGA+U method. Zero refers to the Fermi level.

B. Electronic band structure

The calculated scalar-relativistic band structures, atom- and orbital-decomposed densities of states (DOS) for both structures are plotted in Figs. 5 and 6. These results are calculated by the GGA + U method with $U_{Os} = 2.0$ eV, $U_{Ni} = 5.0$ eV, and $U_{Eu} = 4.0$ eV. In the absence of the SOC, both BaEuNiOsO₆ structures are half-metallic. The energy bands near the Fermi level are purely up-spin and made up of the strongly hybridized Os 5d t_{2g} , O p and Eu 4f orbitals. The half-metallicity is consistent with the integer magnetic moment of 11 μ_B per BaEuNiOsO₆ formula. The atom- and orbital-decomposed DOSs of both structures show that Os 5d t_{2g} orbitals overlap strongly with Eu 4f orbitals and extend to the neighboring Ni 3d orbitals through their hybridization with O p orbitals. This explains the large J_1 (Ni-Os) and J_4 (Eu-Os) values, which give rise to the higher T_c , as mentioned above.

Generally speaking, the SOC has significant effect on the electronic and magnetic properties of these 4f and 5d metal perovskite materials. To find the magnetization orientation of the FM state, we also perform the total energy calculations with the SOC for magnetization along the (001), (110), and (111) directions in bulk BaEuNiOsO₆, and also for (001) and (100) directions in the (111) BaEuNiOsO₆ ML. The easy magnetization axis

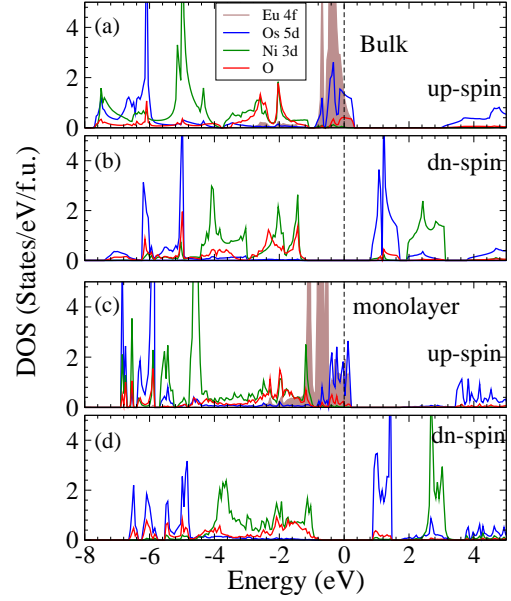


FIG. 6: Atom- and orbital-decomposed densities of states (DOS) of (a, b) bulk BaEuNiOsO₆ and (c, d) the (111) (BaEuNiOsO₆)/(BaTiO₃)₁₀ superlattice obtained with the GGA+U method. Zero refers to the Fermi level.

is found along the (111) direction in bulk BaEuNiOsO₆. Interestingly, the easy axis remains unchanged in the (111) BaEuNiOsO₆ monolayer (along the c axis, see Fig. 2), i.e., the (111) BaEuNiOsO₆ monolayer has a perpendicular anisotropy. This may be useful for realizing high T_c QAH phase in the material.

The fully relativistic FM band structures of both systems with the magnetization along the easy axis are shown in Fig. 7. Interestingly, Fig. 7(a) indicates that linear band crossings appear at the Fermi level in bulk BaEuNiOsO₆ when the SOC is turned on. This makes BaEuNiOsO₆ a candidate for Weyl semimetal. On the other hand, when the SOC is switched on, its (111) monolayer becomes an insulator with a small band gap of 93 meV, thus making it a candidate for a FM topological insulator (or Chern insulator).

The calculated spin and orbital magnetic moments of both systems in the FM state are listed in Table II, together with Eu 4f-, Ni 3f- and Os 5d-shell configurations. Due to the strong SOC effect, the calculated spin magnetic moments fall short of the values expected from Os⁶⁺ 5d² ($t_{2g}^2 e_g^0$; $S = 1$), Eu²⁺ 4f⁷ (f^7 ; $S = 7/2$), and Ni²⁺ 3d⁸ ($t_{2g}^6 e_g^2$; $S = 1$) ions. In particular, the calculated spin magnetic moment of an Os atom is 1.499 μ_B in bulk BaEuNiOsO₆ and 1.463 μ_B in its (111) ML. Interestingly, all Ni, Os, and Eu atoms have significant orbital magnetic moments, being 0.213 μ_B , -0.367 and -0.473 μ_B in bulk BaEuNiOsO₆, and 0.209 μ_B , -0.345 μ_B , -0.566 μ_B in the (111) ML. Hund's second rule states that the spin and orbital moments would be antiparallel if the d or f shell is less than half-filled, and otherwise they would be

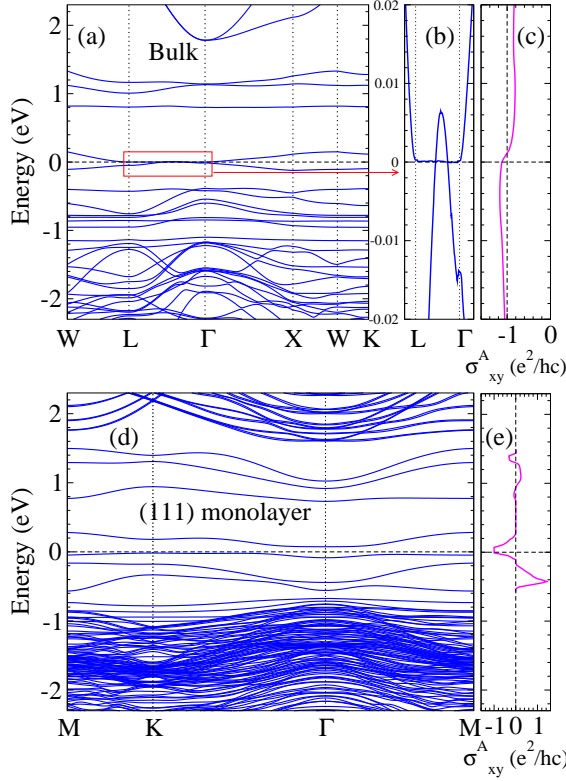


FIG. 7: (a,b,d) Relativistic band structures and (c,d) anomalous Hall conductivity (σ_{xy}^A) of bulk BaEuNiOsO₆ (upper panels) and its (111) (BaEuNiOsO₆)/(BaTiO₃)₁₀ superlattice (lower panels) obtained with the GGA+U+SOC method. Zero refers to the Fermi level.

TABLE III: Position coordinates (in units of $\frac{2\pi}{a_0}$) and chiralities of the Weyl points in bulk BaEuNiOsO₆. Also listed is the momentum separation q^c (also in units of $\frac{2\pi}{a_0}$) along the [111] direction between the two Weyl points in each pair. Here $a_0 = 8.0060$ Å is the lattice constant of cubic BaEuNiOsO₆.

pair	positions	chirality	q^c
1	(0.0740, 0.0740, 0.0740)	+1	-0.2563
	(-0.0740, -0.0740, -0.0740)	-1	
2	(0.2349, 0.2349, 0.2349)	-1	-0.9183
	(0.7651, 0.7651, 0.7651)	+1	

parallel. In consistence with Hund's second rule, the Ni orbital moment is parallel to the Ni spin moment while the Os and Eu orbital moments are antiparallel to their spin moments.

C. Magnetic Weyl semimetal phase

As mentioned above in Sec. III (B), linear band crossings appear at the Fermi level in bulk BaEuNiOsO₆ when the SOC is turned on [Fig. 7(a)], suggesting that bulk BaEuNiOsO₆ is a candidate for the magnetic WSM. One

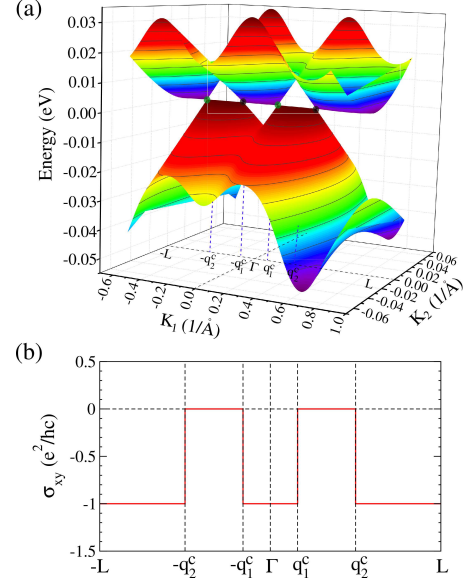


FIG. 8: (a) Energy bands near the Weyl points on the k -plane containing the $-L-\Gamma-L$ line in the Brillouin zone (BZ) in bulk ferromagnetic BaEuNiOsO₆ with [111] magnetization. (b) AHC (σ_{xy}) on the 2D k -plane perpendicular to [111] in the BZ as a function of k_{111} along the $-L-\Gamma-L$ line. See Table IV for the values of critical k -points q_1^c and q_2^c .

characteristic of a WSM is the emergence of pairs of Weyl points with the two Weyl points in each pair having opposite chiralities (chiral charges). Therefore, we first determine the locations and chiralities of the Weyl points in bulk BaEuNiOsO₆. The position coordinates and chiralities of the Weyl points found in bulk BaEuNiOsO₆ are listed in Table III, and their locations and associated Weyl cones are displayed in Fig. 8. In contrast to many previously predicted WSMs [6], there are only two pairs of Weyl points locating at $\pm(0.0740, 0.0740, 0.0740)$ and $\pm(0.2349, 0.2349, 0.2349)$, respectively. Furthermore, they are all located on high symmetry line $-L-\Gamma-L$ in the BZ. Note that for the [111] magnetization in bulk BaEuNiOsO₆, there is a three-fold rotation symmetry (C_{3v}) along this $-L-\Gamma-L$ symmetry line. Consequently, according to the two-band $\mathbf{k}\cdot\mathbf{p}$ theory analysis [65], the four Weyl points found on this symmetry line are protected by the symmetry of crystallographic point group C_{3v} . This is the same as in the case of cubic spinel HgCr₂Se₄ with the magnetization along the [111] direction [65]. However, HgCr₂Se₄ is not an ideal Weyl semimetal because its Weyl points are located at ~ 9 meV above the Fermi level and also there are several nontopological bands at this energy level [18].

Since Berry curvatures in the vicinity of the Weyl points are large [6], one would expect a strong AHE in a magnetic WSM with the Fermi level close to the Weyl points. Therefore, we compute the intrinsic AHC in bulk BaEuNiOsO₆ as a function of the Fermi level, and the result is displayed in Fig. 7(c). Indeed, the calculated AHC

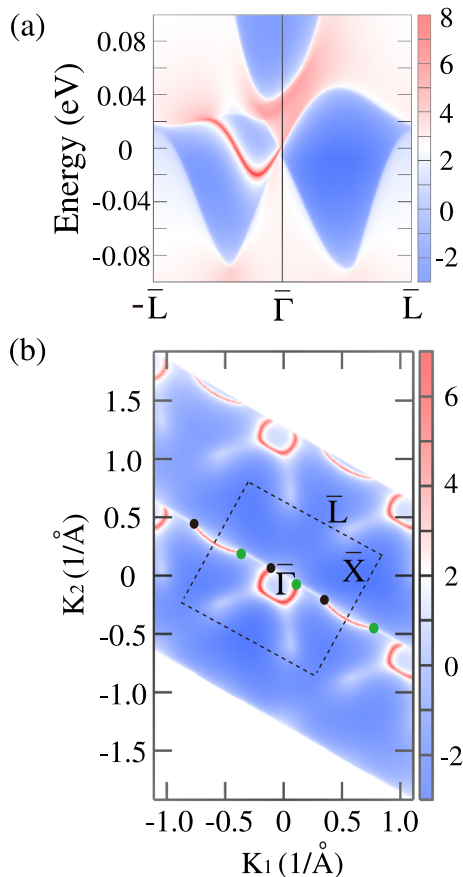


FIG. 9: The (001) surface states of bulk BaEuNiOsO₆. (a) Energy dispersion of the surface states along high symmetry line $-\bar{L}-\bar{\Gamma}-\bar{L}$ in the surface Brillouin zone (BZ) [see Fig. 1(c)]. (b) Surface state spectral function with the energy lying at Weyl points. Here Weyl points with positive and negative chiralities are represented by the black and green solid circles, respectively. The dashed square indicates the surface BZ [see Fig. 1(c)].

at the Fermi level is large, being $-543 \text{ S/cm} = -1.1225 e^2/ha_0$ [see Fig. 7(c)] where e^2/ha_0 is the quantum of the Hall conductance (here $1 e^2/ha_0 = 484 \text{ S/cm}$) and a_0 is the lattice constant of the cubic BaEuNiOsO₆. In retrospect, this is not surprising since bulk BaEuNiOsO₆ is an ideal Weyl semimetal with just two pairs of Weyl points and no other band crossing the Fermi level. It was shown in Ref. [45] that for an ideal magnetic Weyl semimetal, the AHC would be given by

$$\sigma_{ab}^A = \epsilon_{abc} \frac{e^2}{2\pi h} \sum_i q_i^c, \quad (2)$$

where q_i^c is the [111] component of the momentum separation vector of Weyl point pair i , and i is summed over all Weyl point pairs. Using the calculated q_i^c values listed in Table III, we get $\sigma_{ab}^A = -1.1746 \frac{e^2}{ha_0} = -569 \text{ S/cm}$, in good agreement with the *ab initio* calculation. Interestingly, Fig. 5(a) indicates that bulk BaEuNiOsO₆ is half-metallic with the conduction bands being purely spin-up.

Therefore, we expect that the large anomalous Hall current in BaEuNiOsO₆ would be fully spin-polarized.

Another characteristic feature of a WSM is the occurrence of the topological surface Fermi arcs. We thus calculate the band diagram of the (001) surface of bulk BaEuNiOsO₆, as displayed along high-symmetry line $-\bar{L}-\bar{\Gamma}-\bar{L}$ in Fig. 9(a). One surface band connecting the bulk conduction and valence bands along the $-\bar{L}-\bar{\Gamma}$ line can be clearly seen [see Fig. 9(a)]. We also display the spectral function of the surface states at the energy of the Weyl points over the surface BZ in Fig. 9(b). Perfect surface Fermi arc states can clearly be seen and the surface Fermi arcs begin and end at the Weyl points with opposite chirality (labeled by the green and black circles) in Fig. 9(b). Importantly, the surface Fermi arc that connects the Weyl points of pair 2 is long, extending about 68 % of the [111] reciprocal lattice vector (see Table III). It is worthwhile emphasizing that the Weyl points are located right at the Fermi level. Therefore, the WSM states in bulk BaEuNiOsO₆ could be easily detected by such surface techniques such as ARPES and scanning tunneling microscopy (STM). More importantly, many exotic quantum phenomena predicted for WSMs [6] should be observed in FM BaEuNiOsO₆ at high temperature because it is an ideal WSM. We also display the calculated band diagram of the (111) surface in Fig. S2(a) in the SM [49] and also the spectral function of the surface states at the Fermi level in Fig. S2(b) in the SM. Figure S2(a) shows that one surface band crossing the Fermi level and connecting the bulk conduction and valence bands along both the $\bar{M}-\bar{\Gamma}$ and $\bar{\Gamma}-\bar{M}$ lines. However, there are only closed circular surface states [Fig. S2(b)]. There is no surface Fermi arc on this surface because all the Weyl points which are on the $-\bar{L}-\bar{\Gamma}-\bar{L}$ line, now are underneath the surface BZ center (the $\bar{\Gamma}$ point) [see Fig. 1(d)].

D. Chern insulator phase

As mentioned above, the (111) BaEuNiOsO₆ ML is half-metallic in the absence of the SOC [Fig. 5(b)]. However, it becomes a semiconductor when the SOC is included. Thus, we could expect that the SOC-opened band gap in the ML would be topologically nontrivial. To examine the topological nature of the band gap, we calculate the AHC (σ_{xy}^A) [see Eq. (1)] of this monolayer. For a Chern insulator, $\sigma_{xy}^A = ne^2/hc$ where c is the lattice constant along the c -axis normal to the plane of longitudinal and Hall currents and n is an integer known as the Chern number [66, 67]. For a normal FM insulator, on the other hand, $\sigma_{xy}^A = 0$. The calculated AHC of the (111) BaEuNiOsO₆ ML is displayed as a function of the Fermi level in Fig. 7(e). Interestingly, when the Fermi level falls within the band gap, $\sigma_{xy}^A = -1e^2/hc$ [Fig. 7(e)]. This shows that it is a Chern insulator with Chern number $n = -1$. Equation (1) shows that the nonzero Chern number is due to the nonzero Berry curvature of the occupied bands caused by the simultaneous

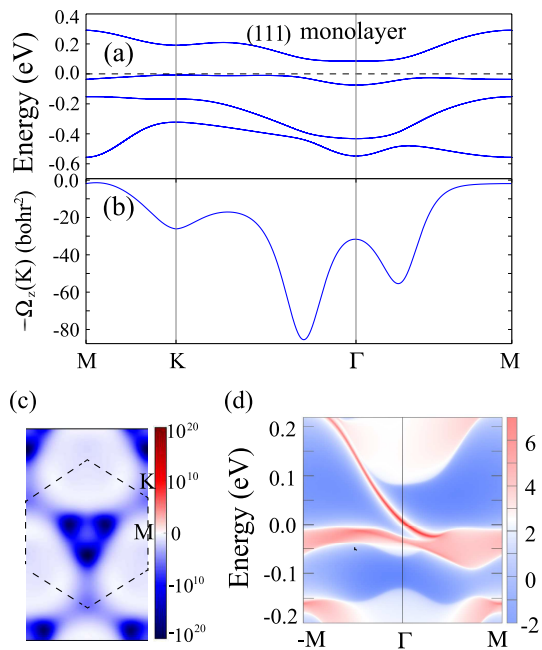


FIG. 10: (a) Relativistic band structure near the Fermi level, (b) Berry curvature along the symmetry lines and (c) distribution of the Berry curvature on the $k_z = 0$ plane in the BZ of the (111) BaEuNiOsO₆ ML in the (BaEuNiOsO₆)/(BaTiO₃)₁₀ superlattice. (d) The edge band diagram of the ML with the edge along the (010) direction.

occurrence of the magnetization and SOC [55]. To locate the hot spots of the Berry curvature in the BZ, we display the Berry curvature along the symmetry lines in Fig. 10(b) and also on the $k_z = 0$ plane in Fig. 10(c). Figure 10(b) shows that the Berry curvature has a prominent negative peak along the K-Γ line near the Γ point. In fact, because the BZ has a three-fold rotation axis at the Γ point, there are three such peaks in the vicinity of the Γ point [see Fig. 10(c)].

According to the bulk-edge correspondence theorem, the monolayer should have one chiral gapless edge mode since its Chern number $n = -1$. To verify this finding, we calculate the edge energy bands along the (010) direction, as spectral functions plotted in Fig. 10(d). There is clearly one metallic edge band emerging within the band gap, being in accordance with the calculated Chern number $n = -1$. Furthermore, this topological band gap is opened in the purely up-spin bands [see Fig. 5(b)]. Thus, it is a single-spin topological semiconducting phase and the edge current would be fully spin-polarized [68]. In retrospect, that the (111) BaEuNiOsO₆ ML superlattice is a Chern insulator should not come as a surprise because it is the (111) quantum-well structure of bulk BaEuNiOsO₆. Like cubic spinel HgCr₂Se₄ [18], bulk FM BaEuNiOsO₆ is a Chern semimetal. Thus, as a unique physical result characterizing a Chern semimetal, the (111) BaEuNiOsO₆ ML, being a quantum-well structure of bulk BaEuNiOsO₆, should be a Chern insulator. [18]

To ensure that this topological property found in

the (111) BaEuNiOsO₆ ML is robust against the thickness variation of the insulating BaTiO₃ layer, we further perform the calculations for the (111) (BaEuNiOsO₆)/(BaTiO₃)₇, (BaEuNiOsO₆)/(BaTiO₃)₁₃ and (BaEuNiOsO₆)/(BaTiO₃)₁₆ superlattices. We find that all the three superlattices have a band structure almost identical to that of the (111) (BaEuNiOsO₆)/(BaTiO₃)₁₀ with a slightly different band gap (see Fig. S3 in the SM [49]). Considering the (111) BaEuNiOsO₆ ML could be grown on other insulating oxide substrates such as SrTiO₃, NaTaO₃ and KNbO₃, we also carry out the calculations for the (111) (BaEuNiOsO₆)/(BaTiO₃)₁₀ superlattice with the in-plane lattice strains of -2 %, -1 % and 0.71 %, which correspond, respectively, to the possible lattice mismatch strains when grown on SrTiO₃, NaTaO₃ and KNbO₃ with the theoretically determined cubic lattice constants being 3.946 Å, 3.985 Å and 4.057 Å. We again find that all the strained superlattices have a nearly identical band structure with a slightly changed band gap compared to that of the unstrained (BaEuNiOsO₆)/(BaTiO₃)₁₀ (see Fig. S4 in the SM [49]).

IV. CONCLUSIONS

In conclusion, based on systematic first-principles DFT calculations, we find that the (111) ML (BaEuNiOsO₆)/(BaTiO₃)₁₀ superlattice is a FM Chern insulator with high T_C of about 210 K and also a large band gap of ~ 90 meV. Guided by the strategy of "inverse engineering", we uncover the corresponding bulk BaEuNiOsO₆ to be an ideal FM WSM with above room temperature T_C of around 325 K and two pairs of Weyl points at the Fermi level only. Furthermore, one pair of Weyl points has a large momentum separation, thus giving rise to not only a long (001) surface Fermi arc but also large AHC of 543 S/cm. Analysis of the calculated band structure and also exchange coupling parameters reveal that the strong ferromagnetism in these double perovskite BaEuNiOsO₆ structures is driven by not only the rare nearest-neighbor Ni-Os FM coupling but also Eu-Os FM coupling. Therefore, double perovskite BaEuNiOsO₆ will offer a superior material platform for exploring exotic Weyl fermion physics and its (111) ML superlattices will provide a high temperature quantum phenomena such as quantum anomalous Hall effect. This work is thus expected to stimulate further experimental and theoretical investigations on these interesting materials.

Acknowledgments

H.-S.L acknowledges the support from the National Natural Science Foundation of China under Grant No. 11704046. G.-Y. G. thanks the support from the Ministry of Science and Technology and the National Center for Theoretical Sciences in Taiwan.

-
- [1] H. Weyl, *Z. Phys.* **56**, 330 (1929).
- [2] X. G. Wan, A. M. Turner, A. Vishwanath, and S. Y. Savrasov, *Phys. Rev. B* **83**, 205101 (2011).
- [3] W. Shi, L. Muechler, K. Manna, Y. Zhang, K. Koepf, R. Car, J. v. d. Brink, C. Felser, and Y. Sun, *Phys. Rev. B* **97**, 060406(R) (2018).
- [4] G. E. Volovik, *The Universe in A Helium Droplet* (Clarendon Press, Oxford, 2003).
- [5] B. Yan and C. Felser, *Annu. Rev. Condens. Matter Phys.* **8**, 337 (2017).
- [6] N. P. Armitage, E. J. Mele, and A. Vishwanath, *Rev. Mod. Phys.* **90**, 15001 (2018).
- [7] M. Z. Hasan and C. L. Kane, *Rev. Mod. Phys.* **82**, 3045 (2010).
- [8] B. Q. Lv, H. M. Weng, B. B. Fu, X. P. Wang, H. Miao, J. Ma, P. Richard, X. C. Huang, L. X. Zhao, G. F. Chen, Z. Fang, X. Dai, T. Qian, and H. Ding, *Phys. Rev. X* **5**, 031013 (2015).
- [9] L. X. Yang, Z. K. Liu, Y. Sun, H. Peng, H. F. Yang, T. Zhang, B. Zhou, Y. Zhang, Y. F. Guo, M. Rahn, D. Prabhakaran, Z. Hussain, S. K. Mo, C. Felser, B. Yan, and Y. L. Chen, *Nat. Phys.* **11**, 728 (2015).
- [10] Z. K. Liu, L. X. Yang, Y. Sun, T. Zhang, H. Peng, H. F. Yang, C. Chen, Y. Zhang, Y. F. Guo, D. Prabhakaran, M. Schmidt, Z. Hussain, S.-K. Mo, C. Felser, B. Yan, and Y. L. Chen, *Nat. Mater.* **15**, 27 (2016).
- [11] S.-Y. Xu, I. Belopolski, N. Alidoust, M. Neupane, G. Bian, C. Zhang, R. Sankar, G. Chang, Y. Zhujun, C.-C. Lee, H. Shin-Ming, H. Zheng, J. Ma, D. S. Sanchez, B. Wang, A. Bansil, F. Chou, P. P. Shibayev, H. Lin, S. Jia, and M. Z. Hasan, *Science* **349**, 613 (2015).
- [12] N. Xu, H. M. Weng, B. Q. Lv, C. E. Matt, J. Park, F. Bisti, V. N. Strocov, D. Gawryluk, E. Pomjakushina, K. Conder, N. C. Plumb, M. Radovic, G. Autes, O. V. Yazyev, Z. Fang, X. Dai, T. Qian, J. Mesot, H. Ding, and M. Shi, *Nat. Commun.* **7**, 11006 (2016).
- [13] H. Inoue, A. Gyenis, Z. Wang, J. Li, S. W. Oh, S. Jiang, N. Ni, B. A. Bernevig, and A. Yazdani, *Science* **351**, 1184 (2016).
- [14] X. Huang, L. Zhao, Y. Long, P. Wang, D. Chen, Z. Yang, H. Liang, M. Xue, H. Weng, Z. Fang, X. Dai, and G. Chen, *Phys. Rev. X* **5**, 031023 (2015).
- [15] C.-L. Zhang, S.-Y. Xu, I. Belopolski, Z. Yuan, Z. Lin, B. Tong, G. Bian, N. Alidoust, C.-C. Lee, S.-M. Huang, T.-R. Chang, G. Chang, C.-H. Hsu, H.-T. Jeng, M. Neupane, D. S. Sanchez, H. Zheng, J. Wang, H. Lin, C. Zhang, H.-Z. Lu, S.-Q. Shen, T. Neupert, M. Zahid Hasan, and S. Jia, *Nat. Commun.* **7**, 10735 (2016).
- [16] E. Liu, Y. Sun, N. Kumar, L. Muechler, A. Sun, L. Jiao, S. Yang, D. Liu, A. Liang, Q. Xu, J. Kroder, V. Süß, H. Borrmann, C. Shekhar, Z. Wang, C. Xi, W. Wang, W. Schnelle, S. Wirth, Y. Chen, S. T. B. Goennenwein, and C. Felser, *Nat. Phys.* **14**, 1125 (2018).
- [17] J. Ahn, G.-Y. Guo and N. Nagaosa, *Phys. Rev. X* **10**, 041041 (2020).
- [18] G. Xu, H. Weng, Z. Wang, X. Dai, and Z. Fang, *Phys. Rev. Lett.* **107**, 186806 (2011).
- [19] W. Jiang, H. Huang, F. Liu, J. Wang, and T. Low, *Phys. Rev. B* **101**, 121113(R) (2020).
- [20] M. Hirschberger, S. Kushwaha, Z. Wang, Q. Gibson, S. Liang, C. A. Belvin, B. A. Bernevig, R. J. Cava, N. P. Ong, *Nat. Mater.* **15**, 1161 (2016).
- [21] C. Shekhar, N. Kumar, V. Grinenko, S. Singh, R. Sarkar, H. Luetkens, S. Wu, Y. Zhang, A. C. Komarek, E. Kampert, Y. Skourski, J. Wosnitza, W. Schnelle, A. McCollam, U. Zeitler, J. Kbler, B. Yan, H.-H. Klauss, S. S. P. Parkin, and C. Felser, *Proc. Natl Acad. Sci. USA* **115**, 9140 (2018).
- [22] J. Kubler, and C. Felser, *Europhys. Lett.* **114**, 47005 (2016).
- [23] Z. Wang, M. G. Vergniory, S. Kushwaha, M. Hirschberger, E. V. Chulkov, A. Ernst, N. P. Ong, Robert J. Cava, and B. Andrei Bernevig, *Phys. Rev. Lett.* **117**, 236401 (2016).
- [24] G. Chang, S. Y. Xu, H. Zheng, B. Singh, C. H. Hsu, G. Bian, N. Alidoust, I. Belopolski, D. S. Sanchez, S. Zhang, H. Lin, and M. Z. Hasan, *Sci. Rep.* **6**, 38839 (2016).
- [25] I. Belopolski, K. Manna, D. S. Sanchez, G. Chang, B. Ernst, J. Yin, S. S. Zhang, T. Cochran, N. Shumiya, H. Zheng, B. Singh, G. Bian, D. Multer, M. Litskevich, X. Zhou, S. Huang, B. Wang, T. Chang, S. Xu, A. Bansil, C. Felser, H. Lin, M. Z. Hasan, *Science* **365**, 1278 (2019).
- [26] D. F. Liu, A. J. Liang, E. K. Liu, Q. N. Xu, Y. W. Li, C. Chen, D. Pei, W. J. Shi, S. K. Mo, P. Dudin, T. Kim, C. Cacho, G. Li, Y. Sun, L. X. Yang, Z. K. Liu, S. S. P. Parkin, C. Felser and Y. L. Chen, *Science* **365**, 1282 (2019).
- [27] N. Morali, R. Batabyal, P. K. Nag, E. Liu, Q. Xu, Y. Sun, B. Yan, C. Felser, N. Avraham and H. Beidenkopf, *Science* **365**, 1286 (2019).
- [28] G. Chang, B. Singh, S. Xu, G. Bian, S. Huang, C. Hsu, I. Belopolski, N. Alidoust, D. S. Sanchez, H. Zheng, H. Lu, X. Zhang, Y. Bian, T. Chang, Horng-Tay Jeng, A. Bansil, H. Hsu, S. Jia, T. Neupert, H. Lin, M. Zahid Hasan, *Phys. Rev. B* **97**, 041104(R) (2018).
- [29] D. S. Sanchez, G. Chang, I. Belopolski, H. Lu, J.-X. Yin, N. Alidoust, X. Xu, T. A. Cochran, X. Zhang, Y. Bian, S. S. Zhang, Y.-Y. Liu, J. Ma, G. Bian, H. Lin, S.-Y. Xu, S. Jia and M. Z. Hasan, *Nature Commun.* **11**, 3356 (2020).
- [30] J. R. Soh, F. de Juan, M. G. Vergniory, N. B. M. Schröter, M. C. Rahn, D. Y. Yan, J. Jiang, M. Bristow, P. Reiss, J. N. Blandy, Y. F. Guo, Y. G. Shi, T. K. Kim, A. McCollam, S. H. Simon, Y. Chen, A. I. Coldea, and A. T. Boothroyd, *Phys. Rev. B* **100**, 201102(R) (2019).
- [31] K.-I. Kobayashi, T. Kimura, H. Sawada, K. Terakura and Y. Tokura, *Nature (London)* **395**, 677 (1998).
- [32] J. Mannhart and D. G. Schlom, *Science* **327**, 1607 (2010).
- [33] H. Y. Hwang, Y. Iwasa, M. Kawasaki, B. Keimer, N. Nagaosa and Y. Tokura, *Nature Mater.* **11**, 103 (2012).
- [34] D. Xiao, W. Zhu, Y. Ran, N. Nagaosa, and S. Okamoto, *Nat. Commun.* **2**, 596 (2011).
- [35] H. M. Weng, R. Yu, X. Hu, X. Dai, and Z. Fang, *Adv. Phys.* **64**, 227 (2015).
- [36] K.-Y. Yang, W. Zhu, D. Xiao, S. Okamoto, Z. Wang, and Y. Ran, *Phys. Rev. B* **84**, 201104(R) (2011).
- [37] Y. Weng, X. Huang, Y. Yao, and S. Dong, *Phys. Rev. B* **92**, 195114 (2015).
- [38] Y. Wang, Z. Wang, Z. Fang, and X. Dai, *Phys. Rev. B* **91**, 125139 (2015).
- [39] L. Si, O. Janson, G. Li, Z. Zhong, Z. Liao, G. Koster, and K. Held, *Phys. Rev. Lett.* **119**, 026402 (2017).

- [40] H.-S. Lu, and G.-Y. Guo, *Phys. Rev. B* **99**, 104405 (2019).
- [41] H. K. Chandra, and G.-Y. Guo, *Phys. Rev. B* **95**, 134448 (2017).
- [42] A. M. Cook and A. Paramekanti, *Phys. Rev. Lett.* **113**, 077203 (2014).
- [43] S. Baidya, U. V. Waghmare, A. Paramekanti, and T. SahaDasgupta, *Phys. Rev. B* **94**, 155405 (2016).
- [44] Y. Chen, D. L. Bergman, and A. A. Burkov, *Phys. Rev. B* **88**, 125110 (2013).
- [45] K.-Y. Yang, Y.-M. Lu and Y. Ran, *Phys. Rev. B* **84**, 075129 (2011).
- [46] H.-S. Lu, and G.-Y. Guo, *Phys. Rev. B* **100**, 054443 (2019).
- [47] H. L. Feng, S. Calder, M. P. Ghimire, Y. H. Yuan, Y. Shirako, Y. Tsujimoto, Y. Matsushita, Z. Hu, C.-Y. Kuo, L. H. Tjeng, T.-W. Pi, Y.-L. Soo, J. He, M. Tanaka, Y. Katsuya, M. Richter, and K. Yamaura, *Phys. Rev. B* **94**, 235158 (2016).
- [48] Y. K. Wang, P. H. Lee and G. Y. Guo, *Phys. Rev. B* **80**, 224418 (2009).
- [49] See Supplemental Material at <http://link.aps.org/supplemental/> for supplementary note 1, Tables S1-S2 and Figs. S1-S4.
- [50] J. P. Perdew, K. Burke, and M. Ernzerhof, *Phys. Rev. Lett.* **77**, 3865 (1996).
- [51] P. E. Blöchl, *Phys. Rev. B* **50**, 17953 (1994).
- [52] G. Kresse and J. Hafner, *Phys. Rev. B* **47**, 558 (1993); G. Kresse and J. Furthmüller, *Phys. Rev. B* **54**, 11169 (1996).
- [53] S. L. Dudarev, G. A. Botton, S. Y. Savrasov, C. J. Humphreys and A. P. Sutton, *Phys. Rev. B* **57**, 1505 (1998).
- [54] H. S. Lu, T.-Y. Cai, S. Ju, and C. D. Gong, *Phys. Rev. Applied* **3**, 034011 (2015).
- [55] D. Xiao, M.-C. Chang, and Q. Niu, *Rev. Mod. Phys.* **82**, 1959 (2010).
- [56] X. Wang, J. R. Yates, I. Souza, and D. Vanderbilt, *Phys. Rev. B* **74**, 195118 (2006).
- [57] M. G. Lopez, D. Vanderbilt, T. Thonhauser, and I. Souza, *Phys. Rev. B* **85**, 014435 (2012).
- [58] N. Marzari, A. A. Mostofi, J. R. Yates, I. Souza, and D. Vanderbilt, *Rev. Mod. Phys.* **84**, 1419 (2012).
- [59] M. P. Lopez Sancho, J. M. Lopez Sancho, and J. Rubio, *J. Phys. F* **14**, 1205 (1984).
- [60] M. P. Lopez Sancho, J. M. Lopez Sancho, J. M. L. Sancho, and J. Rubio, *J. Phys. F* **15**, 851 (1985).
- [61] Q. S. Wu, S. N. Zhang, H.-F. Song, M. Troyer, and A. A. Soluyanov, *Comput. Phys. Commun.* **224**, 405 (2018).
- [62] C.-Z. Chang, J. Zhang, X. Feng, J. Shen, Z. Zhang, M. Guo, K. Li, Y. Ou, P. Wei, L.-L. Wang, Z.-Q. Ji, Y. Feng, S. Ji, X. Chen, J. Jia, X. Dai, Z. Fang, S.-C. Zhang, K. He, Y. Wang, L. Lu, X.-C. Ma, Q.-K. Xue, *Science* **340**, 167 (2013).
- [63] H. X. Fu, C. X. Liu, B. H. Yan, *Sci. Adv.* **6**, eaaz0948 (2020).
- [64] C. Tang, C.-Z. Chang, G. Zhao, Y. Liu, Z. Jiang, C.-X. Liu, M. R. McCartney, D. J. Smith, T. Chen, J. S. Moodera, J. Shi, *Sci. Adv.* **3**, e1700307 (2017).
- [65] C. Fang, M. J. Gilbert, X. Dai, and B. A. Bernevig, *Phys. Rev. Lett.* **108**, 266802 (2012).
- [66] B. I. Halperin, *Jpn. J. Appl. Phys.* **26**, 1913 (1987).
- [67] J. Zhou, Q.-F. Liang, H. Weng, Y. B. Chen, S.-H. Yao, Y.-F. Chen, J. Dong and G.-Y. Guo, *Phys. Rev. Lett.* **116**, 256601 (2016).
- [68] Q.-F. Liang, L.-H. Wu and X. Hu, *New J. Phys.* **15**, 063031 (2013).